scientific reports

Check for updates

OPEN

# Formation of nanostructured electrospark-alloyed coatings on the working surfaces of impulse face seals

Oksana Haponova[1,2]✉, Viacheslav Tarelnyk[3], Gennadii Laponog[1], Dariusz Garbiec[4] & Tomasz Mościcki[2]

**Impulse face seals (IFS) are critical components of pumping and compressor equipment operating under high pressures, rotational speeds, and severe thermal and tribological conditions. The durability and reliability of IFS are largely governed by the properties of their working face surfaces, which motivates the development of advanced surface modification technologies. This study investigates the formation of nanostructured surface layers on Armco iron and HS6-5-2 tool steel by electrospark alloying (ESA) with a special technological medium (STM) containing single-walled carbon nanotubes (CNTs). The proposed processing route involved sequential ESA with a molybdenum electrode, application of CNT-containing STM, repeated ESA. The coatings were characterized in terms of microstructure, elemental distribution, surface roughness, microhardness, and wear resistance. Tribological tests were conducted under end-face friction against fluoroplastic, and real-life tests of an impulse gas face seal were performed to evaluate operational performance. The results demonstrate that adding 0.01 wt% CNTs to STM significantly refines the microstructure. A nanostructured coating with a microhardness of up to 1650 HV (for HS6-5-2 steel) was obtained, demonstrating more than a threefold improvement in wear resistance compared to coatings produced without the STM. Real-life tests confirmed stable sealing performance, low leakage, and a favourable thermal regime. The proposed ESA nanostructuring approach effectively improves the wear resistance and service life of impulse face seals in high-load compressors.**

**Keywords** Electrospark alloying, Special technological medium, Carbon nanotubes, Coating, Microstructure, Wear resistance, Impulse face seals, Real-life tests

Impulse face seals (IFS) are among the most efficient types of sealing units used in modern pumping, compression, and power engineering equipment operating over a wide range of pressures, rotational speeds, and temperatures. Their application is particularly relevant for equipment functioning under increased mechanical loads, in aggressive or cryogenic media, as well as under stringent requirements for tightness and environmental safety. Despite a high level of structural and design sophistication, the service life and reliability of impulse face seals are largely determined by the condition and properties of the working face surfaces of the sealing rings. This underscores the importance of research aimed at improving their surface layers.

Figure 1 shows the IFS of the pump scheme. The axially movable ring (1) with enclosed chambers (7) is pressed against the supporting metal ring (4) by spring (3). The supporting ring is rigidly connected to the rotor shaft (5) and rotates with it. During rotation, the tangential channels 8 of the supporting ring 4 connect the chambers 7 with the pressurized sealed cavity, which generates pressure pulses in the chambers. These pulses alter the balance of axial forces and contribute to the formation of a thin lubricating layer between the face surfaces.

[1]Applied Material Science and Technology of Constructional Materials Department, Sumy State University, Kharkivska 116, Sumy 40007, Ukraine. [2]Department of Experimental Mechanics, Institute of Fundamental Technological Research, Polish Academy of Sciences, Pawińskiego 5B, Warsaw 02-106, Poland. [3]Technical Service and Industrial Engineering Department, Sumy National Agrarian University, H. Kondratiieva 160, Sumy 40021, Ukraine. [4]Łukasiewicz Research Network–Poznań Institute of Technology, Ewarysta Estkowskiego 6, Poznań 61-755, Poland. ✉email: gaponova@pmtkm.sumdu.edu.ua

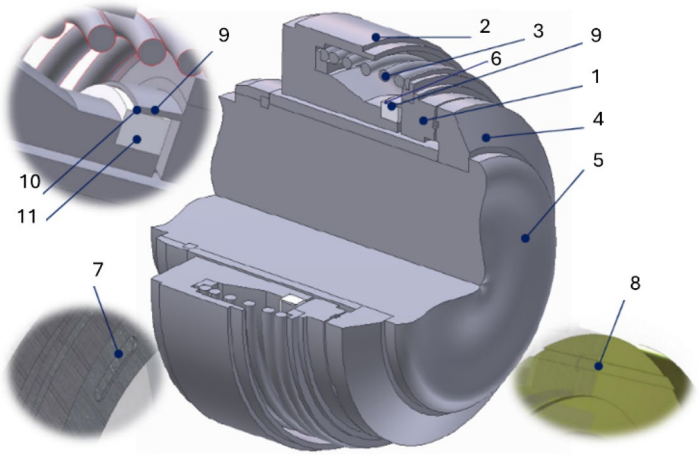


**Fig. 1**. Impulse face seal (IFS) ring of the pump: 1 – axially movable ring; 2 – seal housing; 3 – spring; 4 – supporting metal ring; 5 – rotor shaft; 6 – face surface of ring 1; 7 – chambers; 8 – tangential channels; 9 – secondary seal; 10 – sealed surface of the conical nose; 11 – sealed surface of the sleeve.

IFS operate under conditions of high specific loads, significant circumferential velocities (up to 100 m/s and higher), pressure differentials reaching several tens of megapascals, and within a wide temperature range from cryogenic to elevated temperatures. A characteristic feature of IFS is that, under steady-state operating conditions, the sealing surfaces are separated by a thin layer of the working medium, whereas direct contact between them occurs mainly during start-up and shutdown of the unit. It is precisely these non-stationary regimes that are critical in terms of wear, fretting corrosion, and damage to the surface layers.

The main requirements imposed on the working surfaces of IFS include high wear resistance, a stable low coefficient of friction, corrosion and cavitation resistance, the ability to operate under boundary or mixed lubrication conditions, as well as the preservation of geometric accuracy and surface microrelief over long service periods[1–3]. Traditionally, sealing rings of IFS are manufactured from hard and wear-resistant materials such as tungsten and silicon carbides, graphites, ceramics, as well as high-alloy steels and nickel-based alloys[4,5]. However, using monolithic rings made of these materials significantly increases the cost and complicates the mechanical processing of sealing assemblies. The practice of using IFS shows that it is not necessary to manufacture the entire ring from an expensive material since the thin surface layer absorbs most of the functional load. In this regard, an approach based on the use of metallic substrates followed by the formation of functional coatings that provide the required tribological and operational characteristics is becoming increasingly widespread[6–9].

To improve the wear resistance and service life of IFS, various surface modification methods are widely used in modern technologies. These include physicochemical and physical deposition of coatings[10–12], plasma and ion-plasma treatments[13–16], surfacing processes[17], diffusion-based methods and laser surface texturing[18,19]. PVD (physical vapor deposition) and CVD (chemical vapor deposition) techniques make it possible to form thin, hard coatings with high hardness, a low coefficient of friction, and enhanced corrosion resistance. For example, CVD diamond coatings provide extremely high hardness and low friction, while PVD technologies enable the deposition of multicomponent carbide, nitride or boride layers with a uniform microstructure, which improves the operational performance of parts[11,12,20]. Diffusion-based surface modification methods, such as carburizing, carbonitriding, boriding, and related processes, allow the formation of hard surface layers with increased wear resistance[21]. Laser surface texturing enables the formation of micro- and nanostructures that reduce friction and wear, improve lubricant retention, and enhance the efficiency of sealing systems, especially under conditions of high sliding speeds and pressures[22]. The application of the above-mentioned methods makes it possible to create surface layers that bear the main functional load of face seals, thereby reducing wear of the base material and significantly increasing the overall service life of the sealing unit.

Modern approaches to increasing the service life of IFS include methods based on the use of concentrated energy fluxes. Among them, electrospark alloying is distinguished by a combination of technological flexibility, localized action, the absence of significant thermal loading on the part, and the capability to form multicomponent and multilayer coatings[23–25].

Electrospark alloying (ESA), also widely known as electrospark deposition or electrospark doping, is a pulsed surface modification technique based on short-duration high-voltage electrical discharges between a tool electrode (TE) and the treated surface. In the discharge zone, the TE material melts locally and transfers to the substrate. This process forms a coating with good metallurgical bonding to the base material. The coating is characterized by increased hardness and wear resistance compared to the untreated base substrate[26]. A review of the current state of ESA technologies demonstrates that this method effectively improves the physicochemical properties of surfaces by increasing hardness, wear resistance, and corrosion resistance through the formation of layers with a specific microstructure and phase composition[27]. It has been shown that ESA coatings produced using multicomponent electrodes form mixed crystalline-amorphous structures with high hardness (8.5–15 GPa) and enhanced wear resistance (a reduction in wear losses by up to five times) compared to the substrate material[28].

The application of ESA also enables flexible control of the phase composition and microstructure of coatings. In particular, the use of electrodes containing refractory components and carbides leads to the formation of hard intermetallic phases and carbide compounds within the coating, providing the required tribological properties[28]. Numerous studies have shown that the microstructure of ESA coatings is often represented by nanosized grains or amorphous phases, which contributes to high microhardness and enhanced wear resistance[29,30]. Conventional ESA technology involves the use of electrodes with a predetermined chemical composition, which significantly limits the incorporation of electrically nonconductive or nonstandard components. These limitations have stimulated the development of alternative technological approaches based on the use of a special technological medium (STM) in the form of pastes or viscous compositions applied to the surface prior to treatment. In such methods, an STM containing a binder (polymeric or lubricating bases) and dispersed fillers in the form of metal, nonmetal, carbide, or oxide powders is preliminarily deposited onto the surface. During electrospark discharge, the STM components participate in the substance transfer process within the discharge zone. As a result of intense local heat and mass transfer processes, these components become incorporated and fixed in the surface layer. This approach enables the introduction of electrically nonconductive and nanosized components into the modified surface layer without the need to fabricate special electrodes, while also significantly expanding the possibilities for controlling the phase composition and microstructure of the formed coatings[31,32]. Studies on the role of nanoscale additives in ESA coatings have demonstrated that the incorporation of nanopowders (such as $ZrO_2$, $Al_2O_3$, NbC, WC, and others) leads to a substantial increase in hardness and wear resistance, as well as to an optimized combination of mechanical properties of the surface layers, which is particularly important for the development of tribological coatings[33]. These findings confirm the feasibility of using nanoscale modifiers in the STM composition, including carbon nanotubes (CNTs), for controlled microstructural modification, reduction of the friction coefficient, and enhancement of wear resistance.

However, despite the growing interest in surface nanostructuring by ESA with the use of nanoparticles, previous studies have been primarily focused on the application of nanopowders for the formation of wear-resistant coatings or on the incorporation of nanoparticles directly into the composition of electrode materials. Insufficient attention has been paid to the use of special technological media containing CNTs in the ESA process for controlled nanostructuring of functional surfaces. In addition, the mechanisms of structural evolution and the formation of nanostructured layers during ESA in the presence of carbon nanotubes remain insufficiently investigated. Furthermore, the published results are predominantly of a research nature and are not accompanied by a comprehensive evaluation of the operational performance of the coatings within sealing assemblies. Therefore, the development of new electrospark alloying process routes that combine the use of special technological media with nanoscale components, as well as their experimental and operational assessment under conditions relevant to impulse face seals, represents a scientifically and practically important task.

In this study, a combined technological approach is proposed to improve the operational performance of IFS. The approach involves the use of a steel substrate made of HS6-5-2 tool steel, followed by ESA with molybdenum, application of a STM in the form of a paste containing CNTs, and subsequent repeated ESA with molybdenum. This processing sequence ensures the formation of a gradient quasi-multilayer structure of the surface layer. Previously, the authors conducted systematic studies on the nanostructuring of metallic surfaces by the ESA method, including the incorporation of nanoscale modifiers, which demonstrated a positive effect on the formation of a fine-dispersed microstructure[34]. The obtained results confirm the feasibility of using nanomodifiers in ESA processes for controlled modification of the structure and properties of surface layers of critical parts.

The aim of this paper is a comprehensive investigation of the effect of electrospark alloying using special technological medium containing nanoscale components on the structure and properties of the surface layers of Armco iron and HS6-5-2 steel substrates employed in the manufacture of impulse face seals. Within the framework of this study, changes in microstructure, microhardness, and wear resistance of the formed coatings are evaluated. In addition, full-scale tests are performed on a test rig for gas impulse face seals, which makes it possible to assess the practical effectiveness of the proposed treatment method and its prospects for application under conditions of boundary friction and impulsive loading.

## Materials and methods

Two materials were selected for the research: Armco iron and HS6-5-2 steel. Armco iron was chosen because studying coatings on technically pure iron eliminates the influence of alloying elements on structure formation during ESA. The use of HS6-5-2 steel is explained by its high mechanical properties (hardness, stiffness, etc.), which are required to ensure reliable operation of impulse face seals under conditions of increased mechanical and thermal loads. This choice ensures the practical relevance of the obtained results and their applicability for further industrial implementation.

The chemical composition of the substrate materials and their physicomechanical properties are presented in Tables 1 and 2, respectively.

During the formation of coatings by the ESA method, electrodes made of molybdenum were used. The electrodes were employed in the form of wire: diameter 4 mm, length 20 mm.

Table 3 presents the investigated compositions of STM and electrode materials for obtaining functional coatings by the ESA method. For the dispersion of CNTs in the matrix, the ultrasonic dispersion method was applied according to the technology described in[35]. The composition of STM was selected empirically and is determined by achieving a uniform distribution of nanoparticles in the non-metallic matrix.

ESA was carried out using an Elitron-22 A unit. The experiments were performed at discharge energies of Wp = 0.13 and 0.52 J; the corresponding operating modes are shown in Table 4.

| Alloy grade | Chemical composition, wt% | | | | | | | | |
|---|---|---|---|---|---|---|---|---|---|
| | C | Si | Mn | Ni | S | *P* | Cr | Cu | Other elements |
| HS6-5-2 (1.3339): EN 4957 – 2000 | 0.8–0.88 | max 0.45 | max 0.4 | 9–11 | max 0.03 | max 0.03 | 3.8–4.5 | – | Mo: 4.7–5.2<br>W: 5.9–6.7<br>V: 1.7–2.1 |
| Armco iron | up to 0.025 | up to 0.05 | up to 0.035 | – | up to 0.025 | up to 0.015 | – | up to 0.05 | – |

**Table 1**. Chemical composition of the substrate materials.

| Alloy grade | Heat treatment condition | Microstructure | Hardness |
|---|---|---|---|
| HS6-5-2 | Hardening at 1200–1240 °C with oil quenching, followed by tempering at 540–570 °C | Martensite, retained austenite, carbides | 64–67 HRC |
| Armco iron | As-received condition | Ferrite | 90 HB |

**Table 2**. Physico-mechanical properties of substrate materials used for ESA (cathode).

| Coating | STM composition | Alloying electrode | Cathode material | ESA modes, Wp, J |
|---|---|---|---|---|
| ESA Mo → STM → ESA Mo | Single-walled carbon nanotubes Tuball Ocsial (0.01% by weight) in Epoxy 510 epoxy resin without hardener | Mo | Armco iron | 0.13 |
| | | | HS6-5-2 | |
| | Single-walled carbon nanotubes Tuball Ocsial (0.6% by weight) in Epoxy 510 epoxy resin without hardener | | Armco iron | 0.52 |
| | | | HS6-5-2 | |

**Table 3**. Composition of STM and electrode materials for obtaining functional coatings by the ESA method.

| Type of generator | Capacitance, C, μF | Voltage, U, V | Pulse duration, s | Discharge energy, Wp, J | Productivity, $cm^2$/min |
|---|---|---|---|---|---|
| Transistor–thyristor (TT) | 120 | 75 | $10^{-7}$ – $10^{-8}$ | 0.13 | 1.0–1.3 |
| | 300 | | | 0.52 | |

**Table 4**. Operating modes of the Elitron 52-A unit.

The Armco iron samples were treated according to the following procedure. In the first stage, the surface was subjected to electro-spark alloying using a molybdenum electrode at discharge energies of 0.13–0.52 J, resulting in the formation of an initial modified layer. In the second stage, a special technological medium (STM) containing nanoparticles was applied to the treated surface. The thickness of the STM matched the valleys of the surface roughness that had been formed after ESA. In the third stage, repeated electro-spark treatment was carried out using a molybdenum electrode at the same discharge energy as in the first stage (Fig. 2). The same treatment procedure was applied to the HS6-5-2 steel substrate. For comparison, samples without STM were investigated after alloying with the molybdenum electrode.

Surface roughness was measured using a Talysurf contact profilometer (Taylor Hobson, UK). Roughness profiles were recorded and the arithmetic mean roughness was calculated. For statistical reliability, five measurements were taken for each specimen, and the reported roughness value represents their average. The measurements were conducted in accordance with ISO 21920-2:2021. Vickers hardness measurements and analysis of hardness distribution in the surface layer and as a function of depth from the surface were performed using a NOVA 330/360 hardness tester (INNOVATEST Europe BV, the Netherlands) in accordance with ISO 6507. The maximum applied load was 20 g.

The investigation of microstructural parameters of the coatings was carried out on metallographic cross-sections using the following microscopes: an optical microscope Hirox KH-8700 and a scanning electron microscope SEO-SEM Inspect S50-B equipped with an energy-dispersive spectrometer AZtecOne with an X-MaxN20 detector (Oxford Instruments plc). It should be noted that the coatings are composite. When examining non-metallic materials using a scanning electron microscope, difficulties arise due to the low or zero electron reflectivity. Therefore, a thin gold layer, several angstroms thick, was deposited on the surface. Gold coating of the sample surfaces was performed using a vacuum ion sputtering device (JFC-1100E, JEOL Co., Japan) in an argon atmosphere.

For the identification of structural constituents by metallographic methods, polished sections were prepared from the electrode materials after ESA treatment. To enhance optical contrast between different structural components was achieved by chemical etching of the polished sections using special reagents. The preparation of metallographic specimens, surface finishing, and metallographic examinations were carried out in accordance with established standard procedures[36].

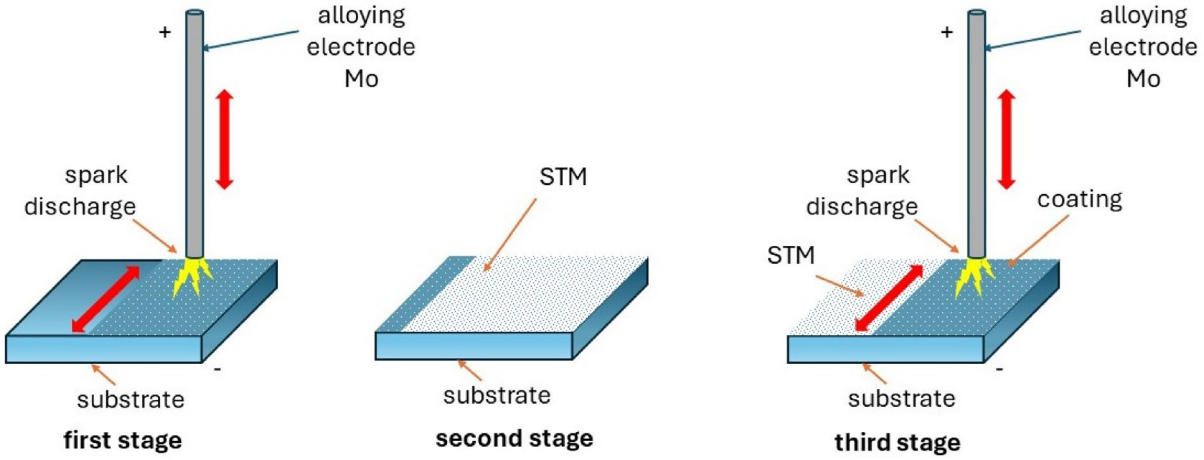


**Fig. 2**. Scheme of the electrospark alloying. The red arrows show the movement of the alloying electrode.

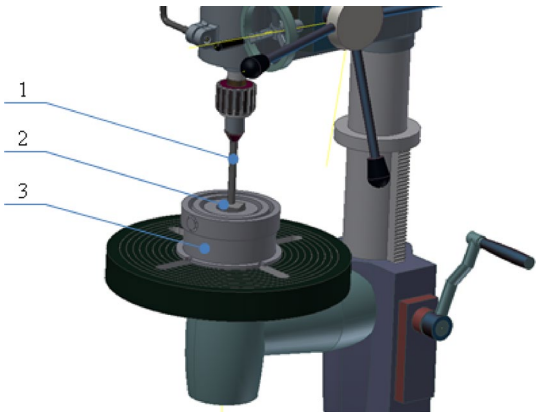


**Fig. 3**. Setup for determining the linear wear of samples under end-face friction:1 – hollow fluoroplastic cylinder counterbody, 2 – rectangular test specimen, 3 – self-alignment fixture for the specimen.

For rapid assessment of the linear wear of coated samples, an experimental setup based on a drilling machine was developed and employed (Fig. 3). The test specimen (2) was fixed in a self-alignment fixture (3) mounted on the machine table, which ensured stable contact and automatic alignment during testing. A hollow cylindrical counterbody (1) made of fluoroplastic F-4K20 (composition: Fluoroplastic-4 (polytetrafluoroethylene) with 20 wt% coke (technical carbon)) was mounted in the machine spindle. The counterbody had an outer diameter of 12 mm, an inner diameter of 4 mm, and a length of 60 mm.

Wear resistance tests were performed on rectangular HS6-5-2 steel specimens with dimensions of $15 \times 15 \times 8$ mm after heat treatment and ESA processing according to the proposed technology. The tests were conducted under end-face friction conditions. Linear wear was determined using the artificial reference marks method, based on the difference in the depths of indentations produced by a Vickers indenter and measured before and after testing. This approach provided sufficient accuracy in determining the wear value. The test duration corresponding to a friction path of 1 km at a spindle rotation speed of 2500 rpm was 16 min and was controlled using a time relay. The total testing time was 320 min. The experiments were carried out at a sliding speed of 1 m/s and a specific load of 4.0 MPa. Wear values were recorded at 64 min intervals throughout the entire test cycle.

## Results and discussion

### Surface topography

A characteristic feature of surfaces after ESA is the formation of a highly developed microrelief caused by local pulsed melting and ultrafast solidification of the material in the zone of action of electrical discharges. This results in the formation of surface protrusions, craters, and regions with increased roughness, creating favorable conditions for the mechanical anchoring and retention of subsequent coatings. This is particularly true for polymer-based composite systems (STM), which are applied in the second stage of treatment. At the third stage of the technological treatment scheme, repeated ESA with a metallic electrode was performed, which

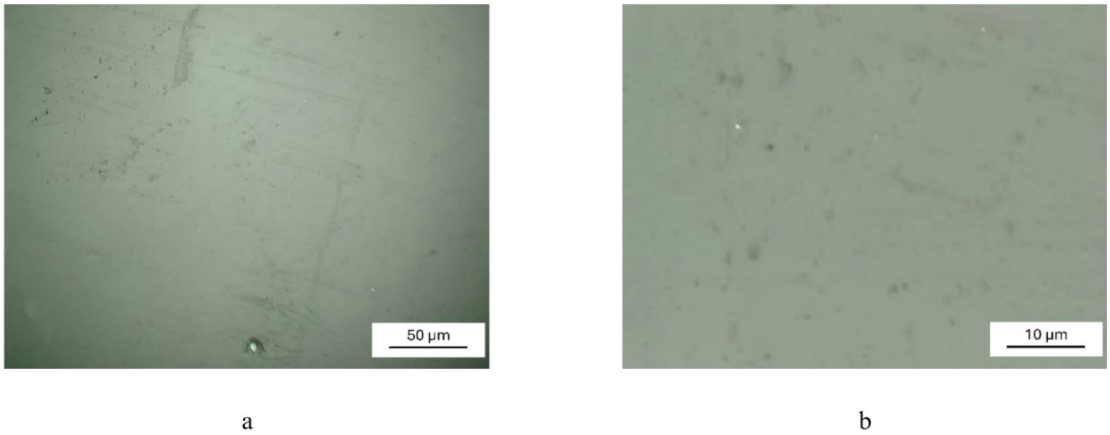


**Fig. 4**. Surface topographies of HS6-5-2 steel samples after processing according to the ESA Mo → STM (carbon nanotubes 0.01 wt%) → ESA Mo scheme at a discharge energy of Wp = 0.13 J: a, b – different magnifications.

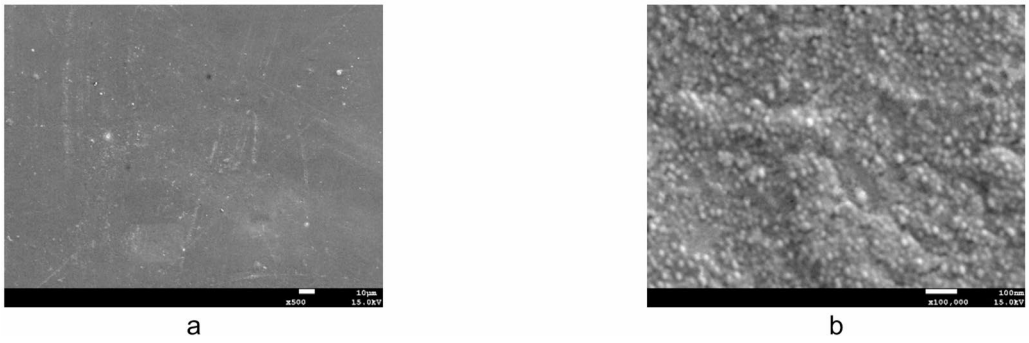


**Fig. 5**. SEM images of the coating surface on HS6-5-2 steel samples after processing according to the ESA Mo → STM (carbon nanotubes 0.01 wt%) → ESA Mo scheme at a discharge energy of Wp = 0.13 J at different magnifications: (**a**) 500×; (**b**) 100,000×.

was accompanied by local melting and mixing of the electrode materials with the components of the STM. At the same time, as is well known, the final surface roughness after ESA is primarily determined by the energy parameters of the process, in particular by the discharge energy. For all samples treated at a discharge energy of Wp = 0.13 J, the roughness values were Ra = 0.98–1.72 μm for Armco iron and Ra = 3.21–3.52 μm for HS6-5-2 steel, whereas at Wp = 0.52 J the roughness was Ra ≈ 1.85 μm for Armco iron and Ra ≈ 3.37 μm for HS6-5-2 steel.

Figure 4 shows the surface topographies of HS6-5-2 steel samples after treatment, obtained using optical microscopy. After the application of STM containing CNTs, regions with increased reflectivity were observed on the surface, indicating sufficient structural homogeneity of the coating and a uniform distribution of the nanofiller in the epoxy matrix. For the sample containing 0.01 wt% CNTs, a uniform distribution of nanotubes over the surface was recorded, which indicates effective dispersion and promotes the formation of a continuous, structurally stable coating with improved adhesion properties.

A high degree of dispersion of CNTs in the STM after ultrasonic treatment is further confirmed by the results of scanning electron microscopy (SEM) (Fig. 5). SEM images obtained at different magnifications reveal nanoscale inclusions with sizes of up to several nanometers, which are uniformly distributed throughout the coating volume without pronounced agglomeration. Such surface morphology confirms the effectiveness of the applied technological scheme and indicates favourable prerequisites for improving the functional performance of the coatings.

## Microstructural analysis

The features of coating structure formation during ESA using STM containing CNTs were analyzed. Metallographic analysis showed that the coatings have a layered structure. A hardened surface layer that resists etching forms on top, followed by a diffusion zone and then the substrate material (Figs. 6 and 7). The microstructure of the substrate is determined by the type of material used. Armco iron has a ferritic structure, while HS6-5-2 steel has a martensitic structure with carbide inclusions.

The microstructural analysis of the coating formed by ESA with a molybdenum electrode without the use of a STM showed that rapid cooling after treatment leads to the formation of a characteristic dendritic structure,

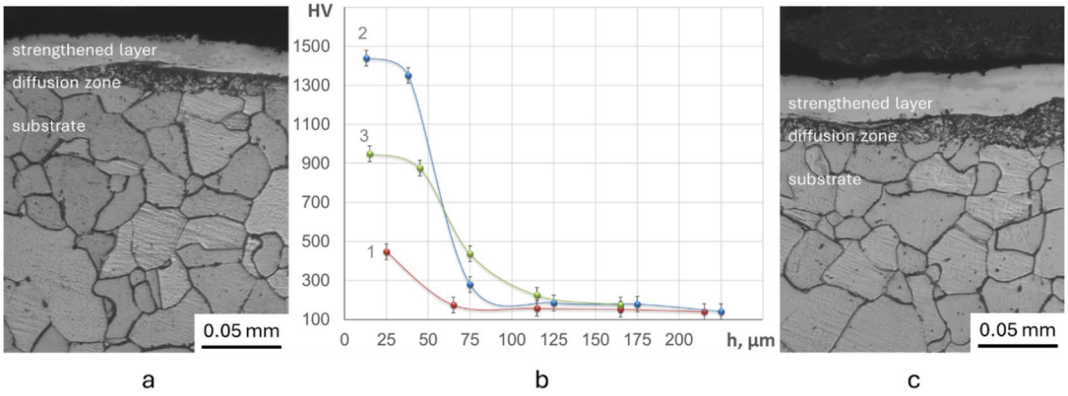


**Fig. 6**. Microstructures (**a**, **c**) and microhardness distribution (**b**) of Armco iron samples after processing according to the ESA Mo → STM → ESA Mo scheme at different discharge energies: (**a**) 0.13 J; (**c**) 0.52 J. In (**b**): 1 – without STM; 2 – coating with STM (carbon nanotubes, 0.01 wt%); 3 – coating with STM (carbon nanotubes, 0.6 wt%).

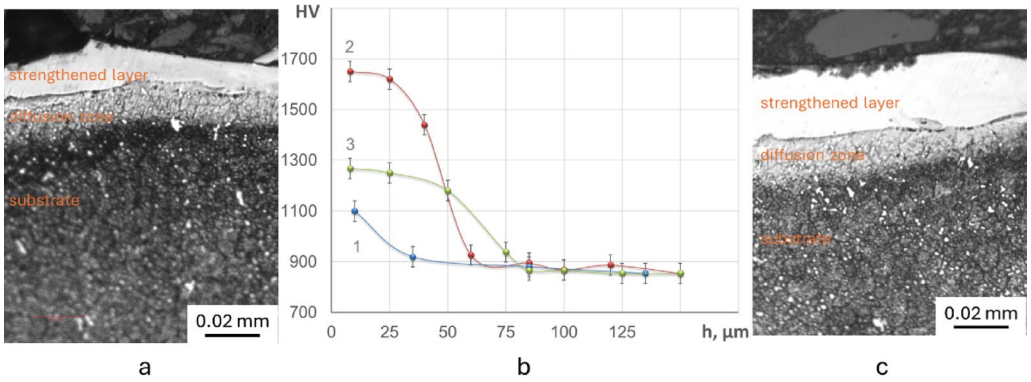


**Fig. 7**. Microstructures (**a**, **c**) and microhardness distribution (**b**) of HS6-5-2 steel samples after processing according to the ESA Mo → STM → ESA Mo scheme at different discharge energies: (**a**) 0.13 J; (**c**) 0.52 J. In (**b**): 1 – without STM; 2 – coating with STM (carbon nanotubes, 0.01 wt%); 3 – coating with STM (carbon nanotubes, 0.6 wt%).

which is clearly revealed at high magnifications in SEM images (Fig. 8). The formation of such a microstructure is typical for the ESA process and is caused by the presence of significant temperature gradients and directional crystal growth during localized pulsed melting of the material followed by ultra-rapid solidification.

Adding CNTs to the STM composition significantly changes the surface morphology and the structure formation mechanisms during ESA, resulting in a change in the crystallization nature of the surface layer. Using STM containing 0.01% nanotubes by mass during ESA results in the appearance of oriented crystals in the microstructure of the surface layer (Fig. 9). This phenomenon is explained by the influence of nanodispersed particles on the number of crystallization centres and the distribution of heat flow in the crystallization zone. In particular, the nanoparticles function as additional heterogeneous crystallization centres, promoting the formation of a large number of crystallites and, consequently, refining the microstructure with a gradual decrease in grain or dendrite size. This mechanism corresponds with literature showing that CNTs can increase crystallization centres and decrease crystallization activation energy, resulting in a finer, more homogeneous nanocomposite structure[37,38]. Studies on nanotube-reinforced composites have shown that the addition of nanotubes promotes the formation of a large number of crystallization centres and limits the growth of individual crystals. This leads to grain boundary strengthening and refinement of the structure[39].

Increasing the concentration of CNTs in STM to 0.6% results in a different structure formation mechanism. Under these conditions, the dendritic structure in the surface layer is not observed (Fig. 10, a), which may be associated with an increase in the number of crystallization centres and a decrease in the crystal growth rate. The significant excess of heterogeneous crystallization centres and the localization of nanotubes at crystal growth boundaries causes the suppression of directed crystal growth since the initial nuclei can no longer grow in a columnar form. In other words, a large number of crystallites nucleate rapidly and simultaneously, and the pinning mechanism blocks their further growth (replacement of growth boundaries by nanotubes, similar to the Zener pinning effect[40]. This results in the formation of a fine crystalline or amorphous dispersed matrix. A

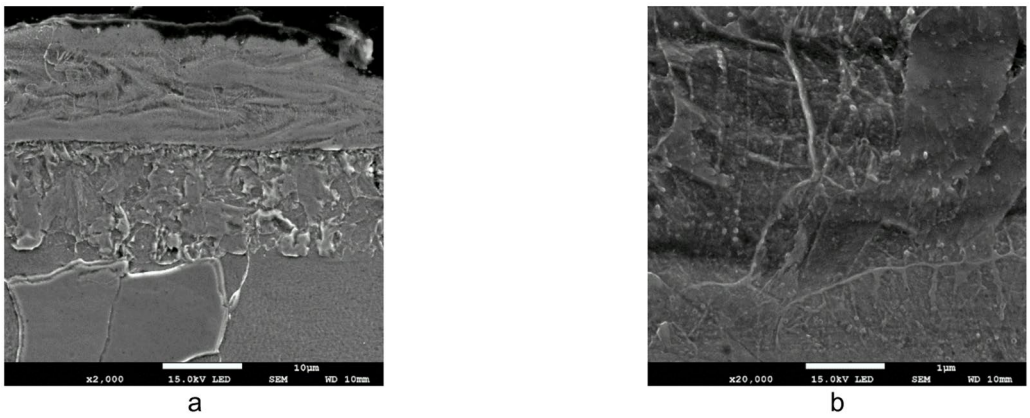


**Fig. 8**. Microstructure of the coating on Armco iron samples after ESA with molybdenum, obtained at a discharge energy of Wp = 0.13 J without STM at different magnifications: (**a**) ×2000; (**b**) ×20,000.

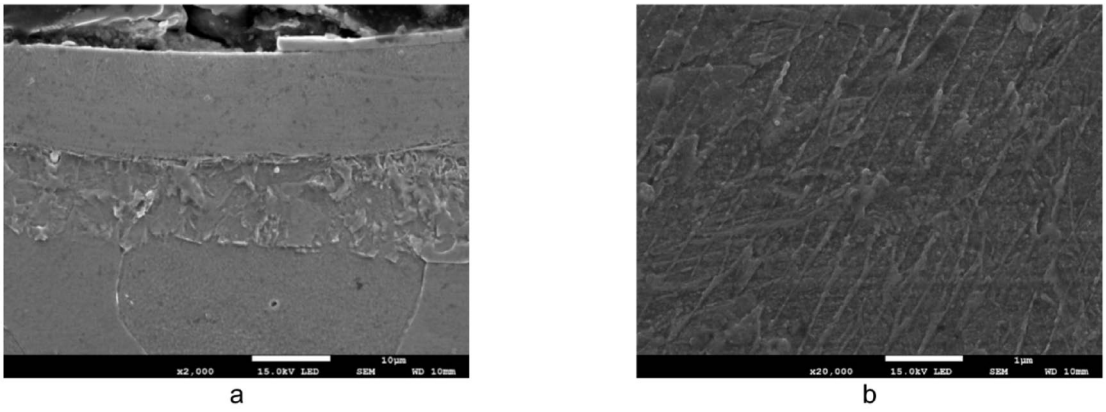


**Fig. 9**. Microstructures of coatings on Armco iron samples after ESA at Wp = 0.13 J using an STM containing carbon nanotubes at 0.01 wt% observed at different magnifications: (**a**) ×2000; (**b**) ×20,000.

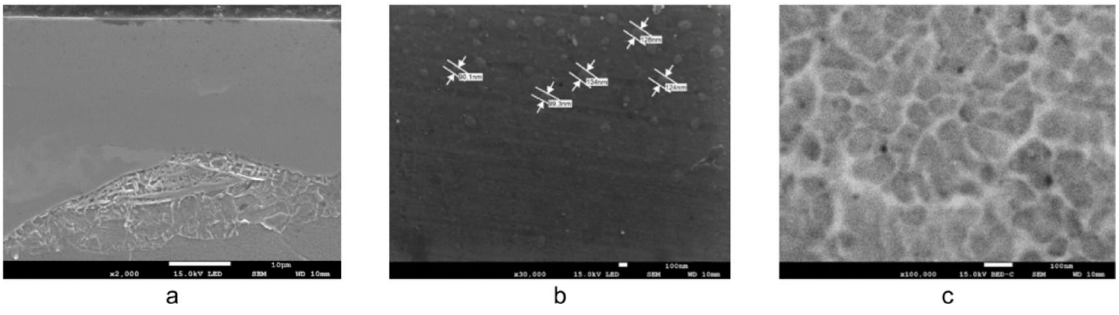


**Fig. 10**. Microstructures of coatings on Armco iron samples after ESA. Mo–STM–Mo coating system obtained at Wp = 0.52 J, STM containing carbon nanotubes (0.6 wt%): magnification (**a**) ×2000; (**b**) ×30,000; (**c**) ×100,000.

similar mechanism has been well described for metal and ceramic nanocomposites in which nanotubes localize at grain boundaries, limiting their growth and resulting in a significant reduction in average grain size and more uniform grain size distribution[41,42].

An increase in the concentration of CNTs above a certain threshold can lead to supersaturation of heterogeneous nucleation sites, which reduces the effective growth of individual crystallites and promotes the formation of a large number of fine inclusions. In our study, ESA treatment with a STM containing CNTs at a concentration of up to 0.6% resulted in the formation of nanoinclusions with sizes of 90–130 nm in a matrix

approaching an amorphous state (Fig. 10b, c). Similar effects have been reported in other nanocomposites, where an increase in CNT content enhanced the heterogeneous nucleation activity while simultaneously limiting the growth of conventional crystalline forms through the generation of numerous nucleation sites and growth-blocking mechanisms[43].

An increase in CNTs concentration above a certain threshold can lead to the supersaturation of heterogeneous nucleation sites. This reduces the effective growth of individual crystallites and promotes the formation of a large number of fine inclusions. In our study, ESA treatment with an STM containing CNTs at concentrations up to 0.6% resulted in nanoinclusion formation with sizes ranging from 90 to 130 nm in a matrix (Fig. 10b, c). Similar effects have been reported in other nanocomposites where an increase in CNTs content enhances heterogeneous nucleation activity while limiting growth of conventional crystalline forms by generating numerous nucleation sites and growth-blocking mechanisms[43].

The elemental distribution maps of carbon, molybdenum, and iron in the surface layer of the samples after ESA at a discharge energy of 0.52 J using a STM containing CNTs are presented in Fig. 11. Analysis of the results shows an intense interaction between the electrode materials and the STM during the ESA process. There was pronounced diffusion of molybdenum into the metallic substrate, accompanied by the formation of a distinct diffusion zone. This confirms the effective alloying of the surface layer. The increased concentration of carbon in the near-surface region may be associated with its stabilization in the surface layer during rapid cooling, as carbon was predominantly introduced from the carbon nanotubes within the STM.

## Hardness and coating parameters

The thickness, continuity, and hardness of the resulting coatings are significantly influenced by the substrate material, STM composition, and discharge energy. The study results showed that the addition of CNTs to the STM at ESA positively affects the formation of a high-quality strengthened surface layer. In particular, the addition of 0.01 wt% of the CNTs to the STM composition significantly increases the continuity, thickness, and microhardness of the strengthened layer. Microhardness increases from 446 to 1438 HV (nearly threefold) for the Armco iron substrate and from 1100 to 1650 HV for the HS6-5-2 steel substrate (Figs. 6b and 7b; Table 5). This increase in hardness correlates with the results of the microstructural study and can be explained by structure refinement and the formation of a fine-grained or quasi-amorphous matrix, as well as possible dispersion strengthening due to the CNTs.

Moreover, the observed microhardness distribution with depth (Figs. 6b and 7b) is explained by the gradient structure of the ESA coatings. The maximum hardness values are recorded in the surface zone, whereas with increasing distance from the surface a gradual decrease to the substrate level is observed. Such behavior is typical for ESA layers and reflects the presence of a strengthened zone, which includes the surface layer and a part of the diffusion zone.

Increasing the CNTs content in the STM to 0.6 wt% does not improve the quality of the coating. In fact, a decrease in microhardness is observed, down to 949 HV for Armco iron and 1267 HV for HS6-5-2 steel (see Table 5). This trend may be associated with the surface layer becoming oversaturated with CNTs, which disrupts the optimal conditions for forming a structure and reduces the effectiveness of dispersion strengthening.

The thickness of the strengthened layer rises in a stepwise manner with rising discharge energy. For instance, for HS6-5-2 steel, the layer thickness is 30–40 μm at a discharge energy of 0.13 J and reaches 60 μm at 0.52 J. This increase is due to the greater volume of molten material and deeper thermal impact at higher ESA energy levels. Meanwhile, STM composition does not significantly impact layer thickness, indicating discharge energy's decisive role in its formation.

The observed changes in microhardness are directly related to the microstructural evolution of the coatings (Figs. 8, 9 and 10). The transition from a pronounced dendritic structure (Fig. 8) to a fine-grained and nanostructured morphology (Fig. 10) results in a significant improvement in mechanical properties. The

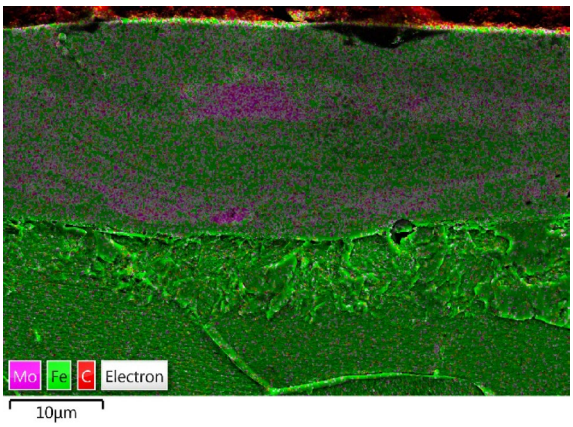


**Fig. 11**. Distribution of elements in the coating obtained at Wp = 0.52 J with STM containing carbon nanotubes (0.01 wt%).

| Electrode Materials / ESA Technology | STM Composition | Wp, J | Thickness of strengthened layer, μm | Microhardness of strengthened layer, HV | Continuity of strengthened layer, % | | Ra, μm | |
|---|---|---|---|---|---|---|---|---|
| | | | | | After ESA | After ESA and NAUFT | After ESA | After ESA and NAUFT |
| Cathode – Armco iron, Anode – Mo ESA Mo → STM → ESA Mo | Without STM | 0.13 | 20–30 | 446 | 65 | 95–100 | 0.98 | 0.2–0.4 |
| | CNTs Tuball Ocsial, (0.01 wt%) in epoxy resin Epoxy 510 without hardener | 0.13 | 30–40 | 1438 | 80 | | 1.72 | |
| | CNTs Tuball Ocsial, (0.6 wt%) in epoxy resin Epoxy 510 without hardener | 0.52 | 40–50 | 949 | 85 | | 1.85 | |
| Cathode – HS6-5-2, Anode – Mo ESA Mo → STM → ESA Mo | Without STM | 0.13 | 15–25 | 1100 | 55 | 90–95 | 3.52 | 0.2–0.4 |
| | CNTs Tuball Ocsial, (0.01 wt%) in epoxy resin Epoxy 510 without hardener | 0.13 | 25–40 | 1650 | 75 | | 3.21 | |
| | CNTs Tuball Ocsial, (0.6 wt%) in epoxy resin Epoxy 510 without hardener | 0.52 | 45–50 | 1267 | 80 | | 3.37 | |

**Table 5**. Parameters and properties of electro-spark coatings. NAUFT – non-abrasive ultrasonic finishing treatment.

refinement of the structure increases the fraction of grain boundaries, which effectively hinder dislocation motion and, consequently, enhance the resistance of the material to plastic deformation.

For the samples treated using STM containing 0.01 wt% CNTs, the formation of a fine-grained microstructure (Fig. 9) leads to a substantial increase in microhardness, reaching 1438 HV for Armco iron and 1650 HV for HS6-5-2 steel (Table 5). This improvement is attributed to the combined effect of grain refinement and dispersion strengthening associated with the uniform distribution of nanoscale inclusions within the surface layer. When the CNT concentration is increased to 0.6 wt%, oversaturation of the surface layer with nanodispersed inclusions is observed (Fig. 10), which reduces the effectiveness of the strengthening mechanisms.

Thus, the variation in microhardness of the investigated coatings is governed by the degree of structural refinement and the stability of the formed nanocomposite structure, which in turn depend on the CNT content in the STM and the ESA parameters.

## Wear resistance results of contacting surfaces in impulse face seals (IFS)

After the formation of the coating by ESA, a significant increase in surface roughness is observed compared to the treated substrate (see Table 5). This increase is a consequence of local melting and solidification under the influence of electrospark. While high surface roughness promotes mechanical interlocking of the STM and the previously applied coating, it may also negatively affect wear resistance performance.

In industrial practice, one of the most effective approaches to reducing surface roughness after ESA is surface plastic deformation (SPD). SPD allows for the modification of surface microtopography without material removal while generating compressive residual stresses in the surface layer. SPD enhances wear resistance and part durability. In the present study, a non-abrasive ultrasonic finishing treatment (NAUFT) was applied to reduce the roughness of the obtained coatings. This process involves the dynamic action of high-frequency mechanical vibrations on the surface without the use of abrasive particles. This treatment induces intense plastic deformation of the surface layer. The result is reduced roughness and the transformation of some of the tensile residual stresses into compressive residual stresses. There is also increased hardness and wear resistance due to structural densification and grain refinement in the surface layer[44].

NAUFT was performed using an ultrasonic generator UZU-030 and an ultrasonic oscillatory system equipped with a single-anvil tool (Fig. 12). The main technical parameters of the ultrasonic system are summarized in Table 6. A deformation tool in the form of a steel ball with a diameter of 5 mm was mounted on the working end of the tip and fixed using a holder. During the strengthening-finishing process, the deformation tool was pressed against the treated surface under a predefined static load. To reduce friction and stabilize the process during NAUFT, the sample surface was lubricated with a fluid containing surfactants. Ultrasonic treatment was carried out under the following technological parameters: static load on the sample $F_s$ = 30 N, amplitude of ultrasonic vibrations of the concentrator $A_{us}$ = 10 μm, frequency of ultrasonic vibrations of the concentrator $f_{us}$ = 18.6 kHz, and feed rate of the sample S = 0.3 m/min.

The study results showed that as a result of NAUFT, the surface roughness parameters decreased.

(Ra = 0.2–0.4 μm), while the hardness simultaneously increased by approximately 20% (Table 5). The observed increase in surface hardness after NAUFT is related to severe plastic deformation of the near-surface layer induced by high-frequency ultrasonic impacts. Similar effects of ultrasonic burnishing have been widely reported in the literature[45]. Such treatment leads to strain hardening, refinement of the surface microstructure, and the formation of compressive residual stresses. These changes result in enhanced surface mechanical properties. The combination of surface densification and grain refinement is considered the main mechanism responsible for the increase in hardness observed after ultrasonic finishing. Therefore, the increase in microhardness after NAUFT can be attributed to the synergistic effect of surface work hardening and microstructural refinement.

Figure 13 shows the dependencies of linear wear Δh of HS6-5-2 steel samples in a friction pair with fluoroplastic over testing time. For all investigated samples, a pronounced increase in wear is observed at the initial stage of testing (up to 64 min), which is associated with the run-in processes of the contacting surfaces.

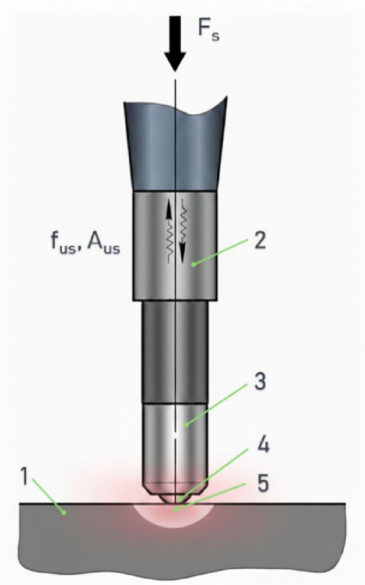


**Fig. 12**. Scheme of non-abrasive ultrasonic finishing treatment (NAUFT): 1 – sample, 2 – ultrasonic concentrator, 3 – single-anvil tip, 4 – tool – ball, 5 – deformation impact zone.

| Supply voltage | Power consumption | Output power | Working frequency | Amplitude of oscillations | Waveform |
|---|---|---|---|---|---|
| 220 ± 10% V | 300 W | 500 W | 18.6 kHz | 10 μm | Rectangular |

**Table 6**. Technical parameters of the ultrasonic generator UZU-030.

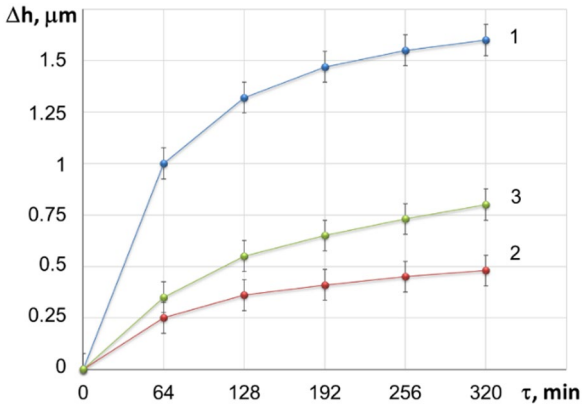


**Fig. 13**. Linear wear of HS6-5-2 steel samples in a friction pair with fluoroplastic: 1 – without STM; 2 – coating with STM (CNTs, 0.01 wt%); 3 – coating with STM (CNTs, 0.6 wt%).

Subsequently, the wear rate decreases, and the Δh(τ) dependencies acquire a quasi-stable character, indicating the establishment of a steady-state friction regime.

The highest linear wear throughout the entire testing period is observed for samples without STM application (curve 1, Fig. 13). After 320 min of testing, the wear reaches approximately 1.6 μm, indicating insufficient wear resistance of the surface layer formed solely by ESA with a molybdenum electrode. The use of STM containing 0.01 wt% CNTs (curve 2, Fig. 13) results in a significant reduction of linear wear at all stages of testing. The final Δh value does not exceed 0.47–0.51 μm, corresponding to a more than threefold decrease in wear compared to samples without STM. This effect can be explained by the formation of a continuous, strengthened coating with increased hardness and the uniform distribution of CNTs in the surface layer.

An intermediate level of wear resistance is observed for samples with 0.6 wt% CNTs (curve 3, Fig. 13). After 320 min, the linear wear is approximately 0.8 μm. This is significantly lower than samples without STM but higher than samples with 0.01 wt% CNTs. An increase in wear at higher CNTs concentrations may be caused by

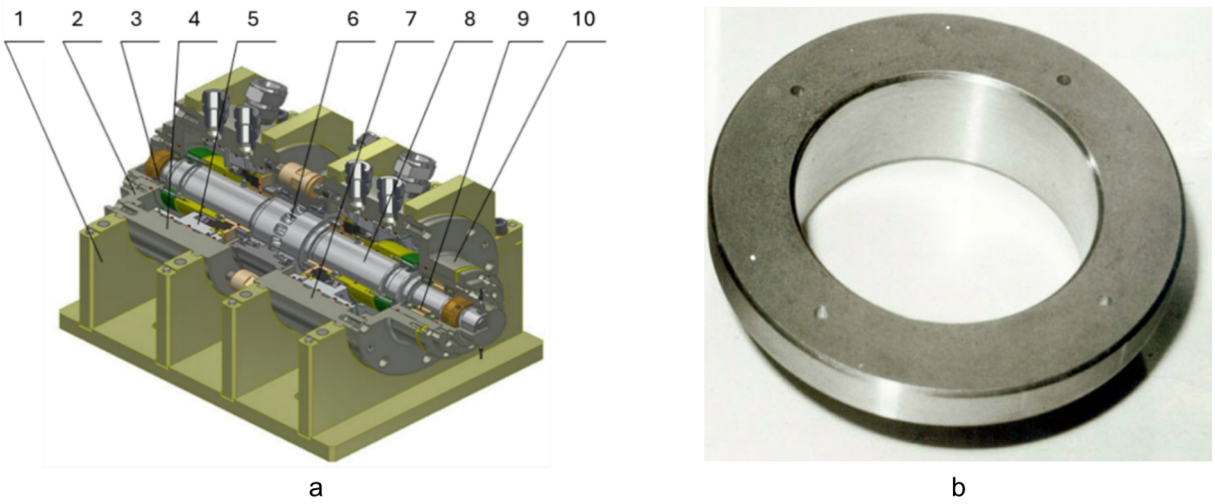


**Fig. 14**. Design scheme (longitudinal section) of the test bench unit (**a**): 1 – outer casing; 2, 10 – covers; 3, 9 – bearings; 4, 7 – inner casing; 5 – impulse gas face seal (IGFS); 6 – turbo drive; 8 – shaft; impulse gas face seal (**b**).

nanoparticle aggregation within the STM, which disrupts the continuity of the coating and reduces its adhesive and mechanical strength.

Thus, the test results confirm that adding carbon nanotubes to the STM composition significantly increases the wear resistance of the HS6-5-2 steel sample surfaces when paired with fluoroplastic for friction. The optimal CNTs content is 0.01 wt%, at which minimum linear wear and a stable friction regime are achieved.

## Real-life tests of an impulse gas face seal

Real-life testing of an impulse gas face seal (IGFS) was conducted to evaluate its performance, tightness, and temperature regime under conditions similar to those of actual compressor equipment operation. The research was carried out for a multiplier compressor for carbon dioxide compression.

The compressor is a four-shaft eight-stage unit in which end seals are installed after the impeller of each stage to prevent $CO_2$ leaks. Operational practice has shown that the standard seals are not sufficiently reliable, particularly at the 5th and 6th compression stages, which leads to their premature wear and unscheduled shutdowns of the unit. In this regard, a new design of a gas end-face impulse seal and a specialised test bench for its real-life testing were developed.

The scheme and design of the test bench are shown in Fig. 14. The bench contains an outer casing, which houses two test chambers for IGFS units. The chambers are formed by an inner casing, end covers and a shaft mounted on radial and radial-thrust bearings. The shaft is rotated by a vortex turbo drive, which provides smooth regulation of the rotation speed in the range of 0–35,000 rpm by changing the buffer gas ($CO_2$) flow rate.

The IGFS operates based on the principle of periodically supplying buffer gas to the chambers during rotor rotation. The pressure of the buffer gas exceeds the pressure of the sealed medium, which changes the balance of axial forces acting on the axially moving ring. This leads to the formation of a gas layer between the working surfaces of the end pair and the formation of a stable end gap, the size of which is automatically adjusted depending on the rotation speed and gas pressure. When there is no rotation, the seal operates in stop mode.

In stop mode, the rings of the IGFS are not subject to wear. At start-up, when the shaft begins to rotate, the contacting surfaces of the rings are compressed against each other and friction occurs for a certain period of time. Until the axially movable ring moves away and a gap appears between the rings, there is the greatest probability of wear on the contact surfaces of the rings. A similar situation occurs when the compressor stops: after the shaft stops rotating, the working surfaces of the rings move closer together and come into contact. At the same time, the surface of the ring rotating with the shaft by inertia rubs against the surface of the axially movable ring for a certain time.

During compressor operation, wear on the working surfaces of the rings is unlikely and mainly occurs if abrasive particles enter the buffer gas. Since the most intense wear occurs during start-up and stop, special attention was paid to start-up modes during testing. Real-life tests of IGFS were carried out with repeated starts and stops, including 20 start cycles over eight hours of compressor operation.

In order to increase the wear resistance, reliability, and service life of the steel rings of the IGFS, ESA technology using STM (Tuball Ocsial CNTs, 0.01 wt%) was applied in this study. The technology involves sequential surface treatment according to the following scheme: ESA with a molybdenum electrode → application of STM → repeated ESA with a molybdenum electrode at a discharge energy of 0.52 J. After ESA, NAUFT was performed to reduce the surface roughness to Ra = 0.2–0.4 μm. The surface hardness of the tested IGFS components was 1950–2000 HV. Adding CNTs to the STM composition creates a strengthened surface layer with increased hardness and a uniform distribution of chemical elements. This improves the tribological characteristics, which is crucial for face seals operating under high pressure and rotational speeds.

Preliminary bench tests showed that the sealing unit ensured stable tightness throughout the entire research cycle, with leakage not exceeding 37 nl/min. The temperature in the friction zone did not exceed 45 °C, indicating a favorable thermal operating mode of the seal. There were no traces of destruction or damage to the coating on the rings' working surfaces.

These results confirm the potential of using a pulsed gas face seal with strengthened surfaces to modernize multiplier compressors for carbon dioxide compression in chemical industry processes.

## Conclusions

1. Impulse face seals (IFS) are widely used in pumping, compressor, and power engineering equipment operating under high loads, variable temperatures, and aggressive environments. The reliability and service life of IFS largely depend on the condition of the working face surfaces, which highlights the relevance of developing effective methods for their modification. In this study, electrospark alloying (ESA) technology using a special technological medium (STM) containing carbon nanotubes (CNTs) was investigated. The technology enables the formation of nanostructured surface layers on iron-based alloy substrates and demonstrates high potential for application in IFS.
2. It was shown that the adding of single-walled carbon nanotubes Tuball Ocsial into the STM composition significantly affects the structure formation mechanisms during ESA. CNTs are effective heterogeneous nucleation centres and inhibit crystal growth, leading to microstructure refinement, formation of fine-grained or quasi-amorphous layers, and a reduction in the pronounced dendritic morphology.
3. The optimal CNT content in the STM was established at 0.01 wt%. Under these conditions, the maximum increase in surface layer microhardness was achieved (up to 1438 HV for Armco iron and up to 1650 HV for HS6-5-2 steel), along with increased coating continuity and a uniform distribution of chemical elements in the near-surface zone. A further increase in CNT concentration to 0.6 wt% results in oversaturation of the surface layer with nanodispersed inclusions, which alters the crystallization behaviour, reduces the effectiveness of dispersion strengthening, and negatively affects the microhardness and tribological properties of the coatings.
4. Tribological tests in the friction pair "HS6-5-2 steel – fluoroplastic" demonstrated that the use of STM containing 0.01 wt% CNTs provides a more than threefold reduction in linear wear compared to coatings formed without STM and promotes a faster transition to a quasi-stable friction regime.
5. Real-life tests of an impulse gas face seal with rings treated using the proposed technology confirmed stable operation of the sealing unit, a low leakage level, and a favourable thermal regime in the friction zone, indicating the practical effectiveness and reliability of the formed coatings.
6. The obtained results demonstrate that electrospark alloying using STM with carbon nanotubes is an effective tool for controlled nanostructuring of surface layers and can be recommended for extending the service life of impulse face seals operating in heavily loaded compressor and power engineering systems.

## Data availability

The datasets used and/or analysed during the current study available from the corresponding author on reasonable request.

Received: 26 February 2026; Accepted: 2 June 2026
Published online: 17 June 2026

## References

1. Lu, P. & Wood, R. J. K. Surface topography characterization and its role in tribology. *Surf. Topogr : Metrol. Prop.* **8**, 043001. https://doi.org/10.1088/2051-672X/abb6d0 (2020).
2. Martsynkovskyy, V., Zahorulko, A., Gudkov, S. & Mischenko, S. Analysis of buffer impulse seal. *Procedia Eng.* **39**, 43–50. https://doi.org/10.1016/j.proeng.2012.07.006 (2012).
3. Tarel'nik, V. B., Martsinkovskii, V. S. & Zhukov, A. N. Increase in the reliability and durability of metal impulse end seals. Part 1. *Chem. Petrol. Eng.* **53**, 114–120. https://doi.org/10.1243/1350650971542408 (2017).
4. Nau, B. S. Mechanical seal face materials. *Proc. Inst. Mech. Eng., Part J: J. Eng. Tribol.* **211**, 165–183 https://doi.org/10.1243/1350650971542408 (1997).
5. He, W., Wang, S., Zhang, C., Wang, X. & Liu, D. Lubrication and wear characteristics of mechanical face seals under random vibration loading. *Materials* **13**, 1285. https://doi.org/10.3390/ma13061285 (2020).
6. Yang, H., Li, S., Ma, R., Zhang, G. & Liu, A. Friction and wear characteristics of Cr–CNTs composite coating end faces of high-temperature mechanical seals. *Coatings* **13**, 1692. https://doi.org/10.3390/coatings13101692 (2023).
7. Simões, R., Martins, B., Santos, J. & Neto, V. HFCVD diamond-coated mechanical seals. *Coatings* **8**, 172. https://doi.org/10.3390/coatings8050172 (2018).
8. Krmela, J., Hovorun, T., Berladir, K. & Artyukhov, A. Increasing the structural strength of corrosion-resistant steel for elastic components of diaphragm compressor. *Manuf. Technol.* **21**, 207–213. https://doi.org/10.21062/mft.2021.034 (2021).
9. Tarelnyk, V., Konoplianchenko, I., Martsynkovskyy, V., Zhukov, A. & Kurp, P. Comparative tribological tests for face impulse seals sliding surfaces formed by various methods. In: (eds Ivanov, V. et al.) Advances in Design, Simulation and Manufacturing, DSMIE 2019, Lecture Notes in Mechanical Engineering, Springer, Cham, 382–391 ; https://doi.org/10.1007/978-3-319-93587-4_40 (2019).
10. Al-Asadi, M. M. & Al-Tameemi, H. A. A review of tribological properties and deposition methods for selected hard protective coatings. *Tribol Int.* **176**, 107919. https://doi.org/10.1016/j.triboint.2022.107919 (2022).
11. Wang, X. et al. A review on tribological wear and corrosion resistance of surface coatings on steel substrates. *Coatings* **15**, 1314. https://doi.org/10.3390/coatings15111314 (2025).
12. Widomski, P. et al. WTaB coatings as effective solutions for increasing die durability in lead-free brass alloy flashless hot forging process. *Wear* **571**, 205849. https://doi.org/10.1016/j.wear.2025.205849 (2025).
13. Lin, N. et al. Surface texturing–plasma nitriding duplex treatment for improving tribological performance of AISI 316 stainless steel. *Materials* **9**, 875. https://doi.org/10.3390/ma9110875 (2016).

14. Ropyak, L. et al. Design of a two-layer Al–$Al_2O_3$ coating with an oxide layer formed by plasma electrolytic oxidation of Al for corrosion and wear protection of steel. *Prog Phys. Met.* **24**, 319–365. https://doi.org/10.15407/ufm.24.02.319 (2023).
15. Pazukha, I. et al. Effect of insulator matrix on electrical transport properties of iron–insulator discontinuous multilayers. *Vacuum* **230**, 113650. https://doi.org/10.1016/j.vacuum.2024.113650 (2024).
16. Hlushkova, D. B. & Volchuk, V. M. Fractal study of the effect of ion plasma coatings on wear resistance. *Funct. Mater.* **30**, 453–457. https://doi.org/10.15407/fm30.03.453 (2023).
17. Lozynskyi, V. et al. Effect of exothermic additions in core filler on arc stability and microstructure during self-shielded, flux-cored arc welding. *Crystals* **14**, 335. https://doi.org/10.3390/cryst14040335 (2024).
18. Tarelnyk, V. B. et al. Effect of laser processing on the qualitative parameters of protective abrasion-resistant coatings. *Powder Metall. Met. Ceram.* **58**, 703–713. https://doi.org/10.1007/s11106-020-00127-8 (2020).
19. Arulvel, S. et al. Laser processing techniques for surface property enhancement: Focus on material advancement. *Surf. Interfaces.* **42**, 103293. https://doi.org/10.1016/j.surfin.2023.103293 (2023).
20. Krella, A. Resistance of PVD coatings to erosive and wear processes: a review. *Coatings* **10**, 921. https://doi.org/10.3390/coatings10100921 (2020).
21. Çep, H. et al. Effects of boriding, nitrocarburizing, nitriding and post-oxidation treatments on the tribological properties of DIN 32CrMoV12-10 steel. *Erzincan Univ. J. Sci. Technol.* **14**, 936–949. https://doi.org/10.18185/erzifbed.959667 (2021).
22. Antoszewski, B. & Kurp, P. Effect of surface texture on the sliding pair lubrication efficiency. *Lubricants* **10**, 80. https://doi.org/10.3390/lubricants10050080 (2022).
23. Al-Quraan, T. M. A. et al. Influence of continuity of electric spark coatings on wear resistance of aluminum alloy. *Tribol Ind.* **43**, 603–614. https://doi.org/10.24874/ti.1170.08.21.10 (2021).
24. Tarelnyk, V., Gaponova, O. & Myslyvchenko, O. Electrospark deposition of multilayer coatings. *Powder Metall. Met. Ceram.* **59**, 76–88. https://doi.org/10.1007/s11106-020-00140-x (2020).
25. Gaponova, O. P. et al. Analysis of the quality of sulfomolybdenum coatings obtained by electrospark alloying methods. *Materials* **14**, 6332. https://doi.org/10.3390/ma14216332 (2021).
26. Młynarczyk, P. et al. The impact of selected ESD parameters on the properties of tungsten layers. *Materials* **18**, 4581. https://doi.org/10.3390/ma18194581 (2025).
27. Wang, J. et al. Research progress in electrospark deposition coatings on titanium alloy surfaces: A short review. *Coatings* **13**, 1473. https://doi.org/10.3390/coatings13081473 (2023).
28. Penyashki, T. et al. Improvement of surface properties of carbon steel through electrospark coatings from multicomponent hard alloys. *Materials* **18**, 2211. https://doi.org/10.3390/ma18102211 (2025).
29. Xie, Y. J. & Wang, M. C. Microstructural morphology of electrospark deposition layer of a high gamma prime superalloy. *Surf. Coat. Technol.* **201**, 691–698. https://doi.org/10.1016/j.surfcoat.2005.12.034 (2006).
30. Barile, C. et al. Advancements in electrospark deposition (ESD) technique: A short review. *Coatings* **12**, 1536. https://doi.org/10.3390/coatings12101536 (2022).
31. Gaponova, O. P. et al. Combined electrospark running-in coatings of bronze parts. Part 1. Structure and mechanical properties. *Metallofiz Noveishie Tekhnol.* **43**, 1121–1138. https://doi.org/10.15407/mfint.43.08.1121 (2021).
32. Haponova, O., Tarelnyk, V., Mościcki, T., Tarelnyk, N. & Kurp, P. Hybrid surface treatment technologies based on the electrospark alloying method: A review. *Coatings* **15**, 721. https://doi.org/10.3390/coatings15060721 (2025).
33. Ma, X., Zhang, D. & Liu, Y. Electro-spark deposition of amorphous and nanostructured coatings: Microstructure and wear behavior. *Surf. Coat. Technol.* **434**, 128159. https://doi.org/10.1016/j.surfcoat.2022.128159 (2022).
34. Gaponova, O. P., Tarelnyk, V. B., Tarelnyk, N. V. & Myslyvchenko, O. M. Nanostructuring of metallic surfaces by electrospark alloying method. *JOM* **75**, 3400–3412. https://doi.org/10.1007/s11837-023-05940-1 (2023).
35. Yasmin, A., Luo, J. J. & Daniel, I. M. Processing of expanded graphite reinforced polymer nanocomposites. *Compos. Sci. Technol.* **66**, 1182–1189. https://doi.org/10.1016/j.compscitech.2005.10.014 (2006).
36. Vander Voort, G. F. *Metallography and Microstructures* (ASM International, 2004).
37. Carneiro, Í. & Simões, S. Strengthening mechanisms in carbon nanotubes reinforced metal matrix composites: A review. *Metals* **11**, 1613. https://doi.org/10.3390/met11101613 (2021).
38. Rubel, R. I., Ali, M. H., Jafor, M. A. & Alam, M. M. Carbon nanotubes agglomeration in reinforced composites: A review. *AIMS Mater. Sci.* **6**, 756–780. https://doi.org/10.3934/matersci.2019.5.756 (2019).
39. Tsai, P. C., Jeng, Y. R., Lee, J. T., Stachiv, I. & Sittner, P. Effects of carbon nanotube reinforcement and grain size refinement on mechanical properties and wear behaviors of carbon nanotube/copper composites. *Diam. Relat. Mater.* **74**, 197–204. https://doi.org/10.1016/j.diamond.2017.03.012 (2017).
40. Mirza, F. A. & Chen, D. L. A unified model for the prediction of yield strength in particulate-reinforced metal matrix nanocomposites. *Materials* **8**, 5138–5153. https://doi.org/10.3390/ma8085138 (2015).
41. Sundaram, R. M., Sekiguchi, A., Sekiya, M., Yamada, T. & Hata, K. Copper/carbon nanotube composites: research trends and outlook. *R Soc. Open. Sci.* **5**, 180814. https://doi.org/10.1098/rsos.180814 (2018).
42. Wang, N., Ji, Y., Wang, Y., Wen, Y. & Chen, L. Q. Two modes of grain boundary pinning by coherent precipitates. *Acta Mater.* **135**, 226–232. https://doi.org/10.1016/j.actamat.2017.06.031 (2017).
43. Qiao, L. et al. Mechanical properties, melting and crystallization behaviors, and morphology of carbon nanotubes/continuous carbon fiber reinforced polyethylene terephthalate composites. *Polymers* **14**, 2892. https://doi.org/10.3390/polym14142892 (2022).
44. Tarel'nik, V. B., Konoplyanchenko, E. V., Kosenko, P. V. & Martsinkovskii, V. S. Problems and solutions in renovation of the rotors of screw compressors by combined technologies. *Chem. Petrol. Eng.* **53**, 540–546. https://doi.org/10.1007/s10556-017-0378-7 (2017).
45. Huuki, J. & Laakso, S. V. Integrity of surfaces finished with ultrasonic burnishing. *Proc. Inst. Mech. Eng. B J. Eng. Manuf.* **227**, 45–53 https://doi.org/10.1177/0954405412462805 (2013).


## Acknowledgements

The authors sincerely thank Vasyl Martsynkovskyy, PhD in Technical Sciences, academician of the Ukrainian Technical Academy, and Director of the TRIZ Ltd, for assistance in conducting real-life tests and valuable consultations regarding the operational testing of impulse face seals.The authors acknowledge the support of the Ministry of Education and Science of Ukraine within the framework of research projects No. 0124U000539, 0125U001429, and the National Research Foundation of Ukraine under project No. 2025.07/0115.

## Author contributions

O.H. : Project administration, Writing – original draft, Writing – review and editing, Conceptualization, Methodology, Investigation, Formal analysis. V.T. : Conceptualization, Methodology, Investigation, Writing – review and editing. G.L. : Investigation, Visualization. D.G. : Investigation, Visualization. T.M. : Methodology, Investigation, Writing – review and editing.

## Funding
No, this research did not receive funding.

## Declarations

## Competing interests
The authors declare no competing interests.

## Additional information
**Correspondence** and requests for materials should be addressed to O.H.

**Reprints and permissions information** is available at www.nature.com/reprints.

**Publisher's note** Springer Nature remains neutral with regard to jurisdictional claims in published maps and institutional affiliations.